catalysts

MDPI

Review

Chemical and Laser Ablation Synthesis of Monometallic and Bimetallic Ni-Based Nanoparticles

Niusha Lasemi and Günther Rupprechter *

Institute of Materials Chemistry, Technische Universität Wien, Getreidemarkt 9/BC, 1060 Wien, Austria; niusha.lasemi@tuwien.ac.at

* Correspondence: guenther.rupprechter@tuwien.ac.at

Received: 6 November 2020; Accepted: 8 December 2020; Published: 11 December 2020

Abstract: The catalytic properties of nanoparticles depend on their size, shape and surface/defect structure, with the entire catalyst performance being governed by the corresponding distributions. Herein, we present two routes of mono- and bimetallic nanoparticle synthesis that enable control of the structural parameters, i.e., wet-chemical synthesis and laser ablation in liquid-phase. The latter is particularly suited to create defect-rich nanoparticles. Impregnation routes were applied to prepare Ni and NiCu nanoparticles, whereas nano- and femtosecond laser ablation in liquid-phase were employed to prepare Ni and NiAu nanoparticles. The effects of the Ni:Cu ratio in impregnation and of laser fluence and liquid-medium on laser ablation are discussed. The atomic structure and (surface) composition of the nanoparticles were characterized by electron microscopic (BF-TEM, DF-TEM, HRTEM) and spectroscopic/diffraction techniques (EDX, SAED, XPS, IR), complemented by theory (DFT). The chemically synthesized bimetallic NiCu nanoparticles initially had Cu-rich surfaces, which changed to Ni-rich upon reaction. For laser ablation, depending on conditions (fluence, type of liquid), highly defective, ordered, or core/shell-like nanoparticles were produced. The case studies highlight the specific benefits of each preparation method for catalyst synthesis and discuss the potential of nanoparticles produced by pulsed laser ablation for catalytic applications.

Keywords: nanoparticle synthesis; pulsed laser ablation in liquids; nickel; nickel-gold; bimetallics; electron microscopy; photoelectron spectroscopy; infrared

1. Introduction

Methane dry reforming is a promising direction of utilizing CO_2, and is thus a topic of intense green energy research [1–3]. Although Ni/ZrO_2 catalysts work well, they suffer from coking, and designing a highly active and coke-resistant catalyst is of importance. Previous studies have emphasized using bimetallic nanoparticles (NPs), due to their modified physicochemical properties, which can be quite different from those of the single elements [4–8]. A central idea is to decorate the sites that lead to coking with less active metals such as Cu or Au. Wet-chemical synthesis is frequently used and the bimetallic nanoparticles often undergo structural/compositional changes during activation and reaction, resulting from the different surface energies of the applied metals.

Laser ablation in liquid (LAL) may serve as an alternative method to produce binary alloy nanoparticles [9–11], particularly for model studies, as structures/compositions may be obtained that are thermodynamically unfeasible and thus not easily accessible by conventional wet-chemical methods. As LAL can be carried out in different (liquid) media, there is still some resemblance to impregnation. To date, a number of binary alloy nanoparticles were produced by nanosecond, picosecond and femtosecond laser ablation in liquids, such as NiAu [12], NiAg [13], AgAu [14–18], FeAu [19], CuAu [14], PtAu [20,21], AgCu [22], AgBi [23], FePt [20], FeW_xO_y [24], and Fe_3O_4Ag [25]. Among the binary alloy NPs, especially binary Cu/M alloys (CuNi, CuZn, CuPt and CuPd) are extensively used

in catalysis, e.g., for methane decomposition (as Cu-rich NPs displayed better coke resistance and easier reducibility of Ni) [8,26–31] and electrochemical CO_2 reduction [32]. Moreover, Au/M alloys (M = Ni [33,34], Cu [8,33], Fe [35], Pt [36], Ag [18] and Pd [37]), specifically NiAu alloy NPs, attracted increased attention due to their altered surface adsorption energy and higher poisoning tolerance. This was stimulated by Besenbacher et al. [38] reporting that a small number of Au atoms on the Ni surface significantly increases the coking resistance [39,40].

Nanoparticle production by pulsed laser ablation in liquids is a comparably new approach that requires the precise selection of parameters based on the photo-physical characteristics of the target materials [41–43]. This is achieved by systematically studying the influence of ablation parameters, such as pulse duration, laser fluence (*F*), applied number of shots (*N*) and the nature of the synthesis environment, on the size distribution, shape, chemical composition and crystallinity of nanoparticles. The complex mechanism of laser ablation in liquid includes a series of processes extending over several orders of magnitude in time (from fs to ms) involving, e.g., photoionization, plasma evolution, cavitation growth, penetration of condensed nano-sized phases into the liquid, cavitation collapse and secondary beam-colloid interactions [44,45]. For more detailed descriptions of the various steps, we refer to reviews [11,43,46].

The first pulsed-laser system (ruby laser) was reported in 1960 [47], in 1987 pulsed laser ablation at the solid/liquid interface was reported by Patil et al. [48], using a Q-switched pulsed ruby laser to ablate an iron target. The main advantage of LAL is that no chemical precursors are required, so that ligand-free surfaces may be obtained [41,49–56]. For catalytic applications, the ablated nanoparticles should have high surface-to-volume ratio and particularly laser-induced high defect densities should promote activity [57–66]. LAL may produce high Miller-index nanoparticle facets with low coordinated sites and introduces crystalline defects (e.g., stacking faults, dislocations, twin boundaries) which leads to additional internal strain [67,68]. In case of Cu nanoparticles, the existence of such stacking faults (SF) plays an essential role to efficiently catalyze methanol formation [69,70]. A high abundance of crystalline imperfections in LAL nanoparticles was reported for nanosecond laser ablated highly-strained Ag nanoparticles (SFs), creating active catalyst for hydrogen evolution by electrochemical water splitting [71].

Additionally, the laser fluence can affect the density of crystalline imperfections. For example, femtosecond laser synthesis of ultrafine-grained Si NPs at relatively high laser fluences showed a higher amount of defect formation (e.g., twining) [72]. Femtosecond pulses are much shorter than the electron-lattice relaxation time (10^{-10} to 10^{-12}) [73], so that rapid cooling of the plasma plum and fast solidification of initial nanoparticles [45] stimulates generation of crystalline defects. Generally, for nanosecond and femtosecond laser ablation in liquids, cooling rates of 10^{10} K/s [74] and 10^{12} K/s [45] are expected, respectively. In the following, chemically- and LAL-synthesized Ni-based catalysts are presented and contrasted to each other, with a focus on (surface) structure and catalytic properties.

2. Results and Discussion

2.1. Wet-Chemical Synthesis of (Partially Oxidized) Ni and NiCu Nanoparticles on ZrO_2

High resolution transmission electron microscopy (HRTEM) analysis of Ni/ZrO_2 revealed monoclinic ZrO_2 particles with a diameter of 50–100 nm (Figure 1a) [75]. Typically, the particles consisted of a face centered cubic (*fcc*) Ni core (Joint Committee on Powder Diffraction Standards (JCPDS) card no. 04-0850) and a disordered shell of several nanometers (Figure 1b,c). According to XRD [75], the shell is NiO (JCPDS card no. 78-0643), which may be partly due to sample air exposure prior to the measurements. The Ni/NiO particles were evenly distributed on the zirconia support and their size ranged from 10 to 30 nm, but most of them had a diameter of ~20 nm. This agrees with a calculated average Ni particle size of 21.5 nm (implying spherical shape), deduced from H_2-chemisorption indicating an accessible metallic Ni surface area of 31.4 m^2/g. When such Ni

nanoparticles are used for reforming reactions [3,8], due to their stepped surfaces, they are very active, but also prone to formation of filamentous carbon, as shown in Figure 1d.

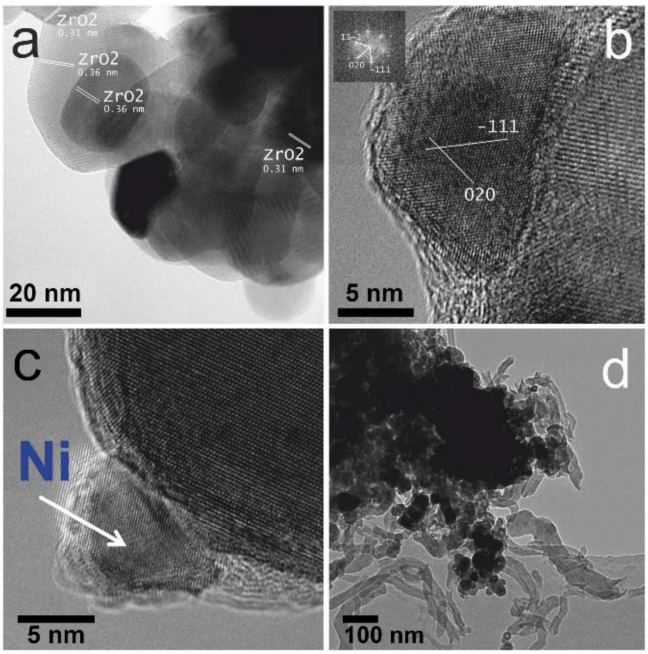

Figure 1. HRTEM micrographs of ZrO_2 supported Ni nanoparticles: Imaging after ex situ oxidation at 773 K followed by reduction at 673 K (sample exposed to air before imaging) reveals (monoclinic) ZrO_2 (**a**) and Ni/NiO particles (**b**) of about 50 and 20 nm diameter, respectively. The Ni nanoparticles may exhibit an NiO overlayer (**c**). After reforming reactions, filamentous carbon is observed (**d**). (**a**,**b**,**d**) Adapted with permission from [75]; published by Springer, 2016. (**c**) Adapted with permission from [3]; published by Elsevier, 2016.

Figure 2a,b show electron micrographs of 1:1 NiCu/ZrO_2 after ex situ reduction. The diameter of the ZrO_2 particles was 50–100 nm, whereas the alloy particles were ~20 nm in size. In order to confirm that NiCu alloy (rather than separated Ni and Cu) nanoparticles formed upon synthesis, various ex situ and in situ methods were applied. Elemental energy-dispersive X-ray (EDX) fluorescence maps proved that the particles contained both Ni and Cu. Because the reduced catalyst was exposed to air prior to TEM/EDX, the NiCu particles are expected to be partially oxidized, which was confirmed by X-ray diffraction (XRD) (JCPDS card no. 65-7246) [29].

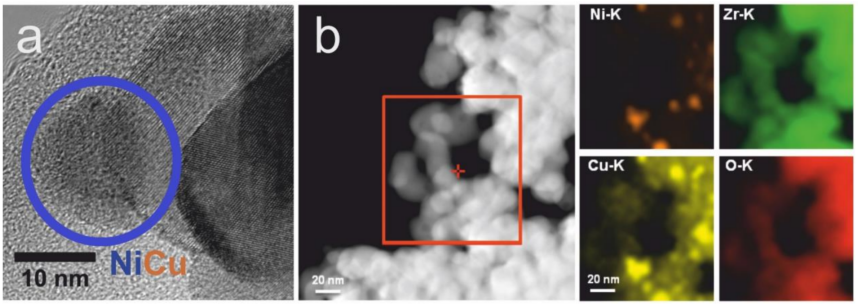

Figure 2. (**a**) HRTEM image of a bimetallic NiCu nanoparticle on ZrO_2. The NiCu particle in the circle was identified EDX. (**b**) Scanning TEM overview and EDX maps of Ni, Cu, Zr and O of the region marked by the red square. Imaging after ex situ oxidation at 773 K followed by reduction at 673 K (sample exposed to air before imaging). Adapted with permission from [8]; published by The Royal Society of Chemistry, 2015.

In addition to electron microscopy, surface-specific methods, such as Fourier transform infrared (FTIR) and near ambient pressure X-ray photoelectron (NAP-XPS) spectroscopy, were employed to characterize the surface composition. Figure 3a shows room temperature FTIR spectra in up to 5 mbar CO and after evacuation to $<2 \times 10^{-6}$ mbar, with the sample pre-reduced in 5 mbar H_2 at 400 °C.

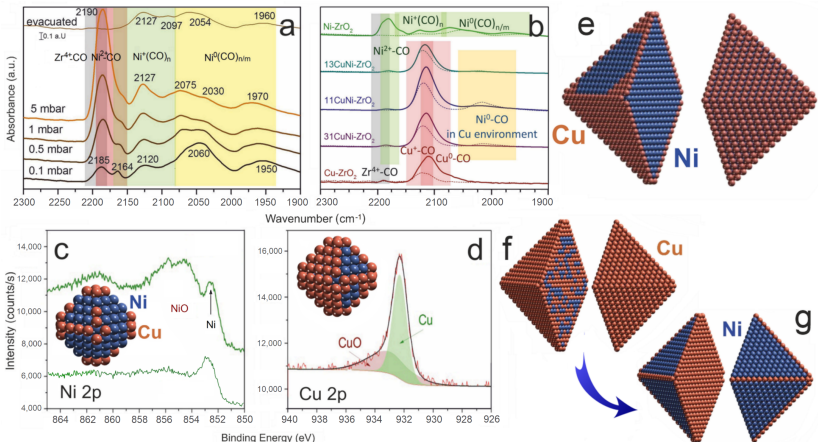

Figure 3. IR and NAP-XPS spectra and DFT-derived models of Ni or NiCu nanoparticles supported by ZrO_2: room temperature IR spectra of (**a**) reduced Ni/ZrO_2 and (**b**) various NiCu/ZrO_2 in up to 5 mbar CO (solid lines) and after evacuation (dashed lines). (**c**) Ni 2p3/2 and (**d**) Cu 2p3/2 in 0.25 mbar H_2 at 400 °C (E_{kin} of ~150 eV; incident photon energies were 1010 and 1100 eV for Ni and Cu, respectively). The lower trace in (**c**) was acquired at 450 °C in methane. Structure models derived by density functional theory (DFT) are shown in (**c**,**d**,**e**), with (**f**,**g**) illustrating Ni segregation to the surface, induced by adsorbed CH_x (2435 Cu atoms and 840 Ni atoms, 3275 atoms in total; color code: Ni—blue, Cu—redwood). (**a**) Adapted with permission from [75]; published by Springer, 2016. (**b**,**e**,**f**,**g**) Adapted with permission from [29]; published by Elsevier, 2017. (**c**,**d**) Adapted with permission from [8]; published by The Royal Society of Chemistry, 2015.

Peaks at 2185–2190 cm^{-1} and 2164 cm^{-1} characterize Zr^{4+}–CO and Ni^{2+}–CO, respectively. With increasing CO pressure, the first grows and obscures the second. The peak at 2060 cm^{-1} and the broad band(s) below 2000 cm^{-1} are due to linearly adsorbed CO and threefold hollow bonded CO on Ni^0, respectively [75–78]. The band at 2120–2127 cm^{-1} originates from Ni^+–CO, resulting from a surface reaction ($Ni^{2+} + Ni^0 \rightarrow 2\ Ni^+$ [79]). CO-FTIR confirms that both oxidized and reduced Ni species are present on the catalyst surface.

These spectra, together with further CO-FTIR of Cu/ZrO_2, provide the basis for characterizing bimetallic NiCu nanoparticles. Figure 3b displays room temperature FTIR spectra in 5 mbar CO (highest pressure selected due to weak CO bonding on Cu), with the samples again pre-reduced at 400 °C. Apart from peaks characterizing CO on reduced Ni and Cu, bands of CO on oxidized Ni and oxidized Cu species are observed, pointing to incomplete reduction. On the monometallic (oxidized) Ni/ZrO_2 sample the typical peaks of Ni^0 and Ni^+ appeared, as discussed before. CO on reduced Cu/ZrO_2 exhibits (apart from the Zr^{4+}–CO interaction at 2190 cm^{-1} [29,80–83]) only a single peak around 2111 cm^{-1}, consisting both of Cu^0–CO and stronger Cu^+–CO contributions. Surprisingly, on all copper containing bimetallics, the typical bands characterizing Ni^0 and Ni^+ are largely absent, whereas the weaker CO interactions with reduced Cu^0 (below 2110 cm^{-1}) [84–87] and Cu^+ (2120–2143 cm^{-1}) are observed [84–86].

Upon alloying Ni and Cu, the Ni^0–CO peak, located at ~2070 cm^{-1} in 5 mbar CO, red-shifts by 50–70 cm^{-1} to 2012–2023 cm^{-1} on the bimetallics (Figure 3b), in line with results of Dalmon et al. [88]. On the bimetallic samples, the CO adsorption on Cu exceeds CO interacting with Ni, suggesting that on the bimetallic surface more Cu than Ni atoms are present. Accordingly, FTIR spectroscopy proved that surface alloy formation occurred, but with Cu surface-enrichmented in Cu, independent of the initial Ni:Cu ratio in the synthesis.

To examine this effect even further, in situ XPS spectra were acquired in the Ni $2p_{3/2}$ and Cu $2p_{3/2}$ regions. Figure 3c displays a spectrum of 31NiCu/$ZrO_2$50, i.e., Ni-rich particles, recorded during reduction in 0.25 H_2 at at 400 °C. The peaks at 854.3 and 852.6 eV in Figure 3c characterize NiO [89–92] and Ni [92,93], respectively (spectra are very similar for Ni NPs). The peak at 932.3 eV in Cu $2p_{3/2}$ characterizes metallic Cu (Figure 3d), the small broader one at 933.3 eV CuO [92,94–97]. Alloying of Ni with Cu cannot be directly proven by XPS, resulting from the small alloying-induced chemical shift of ~0.2 eV [98,99]. However, comparing the peak intensities/areas, it is evident that after synthesis and pretreatment the nanoparticle surface is Cu-rich even for a nominal Ni:Cu ratio of 3:1 (which was catalytically most active [8,75]), corroborating the IR results.

To explain the Cu enrichment, theoretical calculations by density functional theory (DFT) were performed for nanometer sized NiCu NPs, shown as insets in Figure 3c,d, allowing one to determine the optimal chemical ordering (for details see ref [29]). Figure 3c shows the results of DF calculations by Neyman and coworkers for a ca. 1.4 nm $Ni_{105}Cu_{35}$ particle with truncated octahedral *fcc* structure. The nanoparticle has 96 atoms at the surface and 44 atoms in the interior. Cu segregation on surface positions was found energetically favourable. The largest energy gain was obtained for Cu segregation to 6-coodinated corners (−413 meV). Lower energy gain was associated with Cu at 7-coodinated edge positions (−300 meV) and 9-coordinated terrace (−193 meV) sites. This clearly shows that Cu is more stable on the surface relative than in the bulk, preferring corner and edge sites to terrace positions (Figure 3c). When the Cu amount is increased, e.g., in NiCu 1:1, Ni is thus present on the surface solely when the number of Cu atoms in the NP is insufficient to occupy all surface sites, as shown for the minimum-energy structure of $Ni_{70}Cu_{70}$ (inset of Figure 3d).

The descriptors obtained through the precise electronic structure calculations of NPs with 140 atoms also allowed to predict the chemical ordering in larger NPs with truncated octahedral *fcc* structure (~6 nm), which are more similar to the chemically synthesized NPs. Such particles have 3275 atoms in total and 1020 surface positions and exhibit preferential Cu segregation. This is shown in Figure 3e for a $Ni_{2416}Cu_{819}$ (3:1) particle, with a pure Ni interior and Cu occupying 80% of the surface (at 0 K). More precisely, Cu sits at all 24 corner and 156 edge sites, whereas Ni atoms form islands on some of the surface terraces. From 225 to 725 °C, the Ni concentration on the surface nearly doubles (from 20 to 35%), showing that Ni segregation on the surface is facilitated by higher temperature [29]. For $Ni_{1637}Cu_{1638}$ (1:1) and $Ni_{819}Cu_{2416}$ (1:3) (Figure 3f) NPs, at 0 K the outer shell is fully covered with Cu, but even at 725 °C the Ni surface concentration was calculated to be only 15% and 5%, respectively. Thus, the calculations corroborate the experimentally determined Cu-rich surfaces of the NPs after synthesis, even when the NP is overall rich in Ni.

When the NiCu nanoparticles were applied for methane reactions up to 500 °C [8,29], NAP-XPS indiciated that Ni segregated to the surface, replacing the Cu surface atoms (lower trace of Figure 3c,f,g). NAP-XPS also detected various carbonaceous species at the particle surface and DFT calculations revealed that the adsorption of CH_x groups (x = 0–3) provided the driving force for Ni segregation to the surface. CH_3 provides the lowest and C the highest stabilization, in addition to the temperature increase favouring a Ni-rich surface [29].

Taking all effects into account, an "ideal" coking-resistant NiCu alloy particle would consist of edges and corners from Cu, and terraces of Ni, but the interior must be Cu (Figure 3g), so that segregating Ni cannot replace all Cu surface atoms and thus reverse the intended coking resistance. To meet these criteria a ~6 nm large truncated octahedral NiCu nanoparticle should have 840 Ni atoms and 2435 Cu atoms, 3275 atoms in total. After synthesis and pretreatment, the Ni atoms would be mostly located inside the particle (Figure 3f) and only after reaction-induced segregation Ni atoms are on the surface (Figure 3g). Nevertheless, the Ni atoms would just be sufficient to cover the terrace positions on the nanoparticle surface, while the Cu atoms should occupy 180 edge/corner positions and the 2215 interior sites (Figure 3g).

Such an ideal $Ni_{840}Cu_{2435}$ particle corresponds to a 1:3 Ni:Cu composition, which indeed has experimentally shown much better coking resistance [8,29]. According to temperature-programmed

oxidation (re-oxidizing carbon), the amount of coke was about half and it was less-stable (reoxidized at ~100 °C lower temperature) than that formed on Ni/ZrO_2. However, the better coking resistance of 1:3 Ni:Cu was accompanied by a five-fold reduction in activity. Apparently, if most of the active Ni sites (edges, steps, corners) are replaced by Cu, coking is reduced, but at the expense of activity.

2.2. Nanosecond Laser Synthesis of Ni/NiO_x Nanoparticles

Laser ablation of Ni targets in liquid environment is an alternative route of nanoparticle synthesis [55,100–102]. Ni nanoparticles are prepared and collected in the liquid, e.g., ethanol, before they are dropcast on carbon-coated Cu grids for TEM analysis (this facilitates imaging, but oxide supports could also be used). As mentioned, the ablation conditions (pulse length, energy and number) are crucial, but also the type of liquid environment may affect the nanoparticle generation.

Figure 4 shows the effect of increasing nanosecond laser fluence on the size distribution of Ni NPs synthesized in ethanol by 1000 pulses. Table 1 collects the median and mean sizes and the polydispersity indicators. For the lowest fluence of 309 J cm^{-2}, there is a maximum at ~10 nm with some tailing to larger size (diameter), best represented by the median size of 10.6 nm, rather than the simple average of 12.8 nm. The polydispersity in lognormal distributions can be described by the interquartile range (IQR), that is representative of deviations from median sizes [12] (Table 1), whereas standard errors are presented to show deviations from mean values. Such Ni NPs would be well-suited for catalytic studies. With increasing fluence, the median increases up to 20.6 nm, enabling to tune particle size in studies of size effects. This trend agrees with previous experimental and theoretical studies in the nanosecond and femtosecond regime [24,50,55,72,103,104]. The local vaporization of the target forms a high temperature-pressure plasma forming NPs (see Section 3 below). The plasma creates a supercritical temperature liquid that triggers the formation of a cavitation bubble and subsequently of a low-density metal-fluid mixing region [45]. Higher laser fluences lead to a higher plasma temperature, higher temperature in the bubble and subsequently in increased Brownian motions, which increases the NP collisions and thus particle sizes [105]. Accordingly, increasing laser fluence (*F*) resulted in larger median sizes and broader size distribution, due to increased probability of particle-particle collisions. In the studied range, there is even a linear relationship between *F* and the median and IQR values for ns laser-synthesised Ni NPs in ethanol.

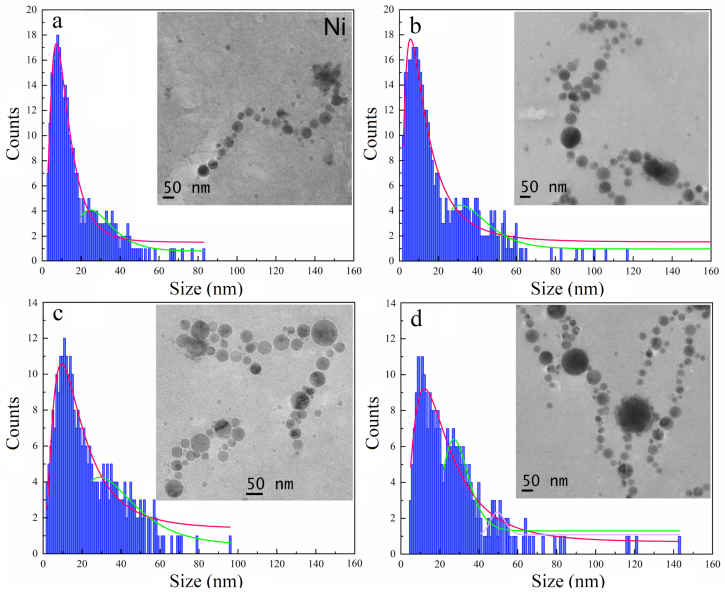

Figure 4. Number weighted size distribution (**a**–**d**) and TEM bright-field images (as insets) of Ni nanoparticles nanosecond laser-synthesized in ethanol (*N*=1000). (**a**) *F* = 309 J cm^{-2}; (**b**) *F* = 486 J cm^{-2}; (**c**) *F* = 663 J cm^{-2}. (**d**) *F* = 840 J cm^{-2}. The red and green lines are LogNormal fits based on the analysis of up to ~400 nanoparticles. Adapted with permission from [55]; published by ChemPhysChem, 2017.

Table 1. The effect of fluid nature and pulse fluence on the size and polydispersity of ns laser-synthesized Ni NPs (N = 1000) [55].

Medium	F (J cm^{-2})	Counted NPs	Mean (nm)	Median (nm)	IQR
Ethanol	309	300	12.8 ± 8.7	10.6	1.0
Ethanol	486	381	17.1 ± 17.8	11.9	2.7
Ethanol	663	301	22.6 ± 20	16.9	4.4
Ethanol	840	268	27 ± 22.8	20.6	5.9
Isopropanol	663	482	16.6 ± 11.7	13.6	2.9
Butanol	663	477	14.5 ± 8.3	12.6	3.4
Water	663	175	17.7 ± 14.2	13.9	5.3

To analyze the structure and composition of the NPs, combined bright-field (BF)/dark-field (DF)-TEM, selected area electron diffraction (SAED) and EDX studies were performed, indicating crystalline *fcc* nickel cores (JCPDS card no. 04-0850) with stacking fault defects, likely surrounded by thin Ni oxide shells (Figure 5) (JCPDS card no. 78-0643). Figure 5b depicts the corresponding SAED pattern, Figure 5c the related dark-field image (for the objective aperture located on the bright Ni spot on the 5th virtual ring in Figure 5b). The dark-field image of one nickel NP, characteristic of a (222) *fcc* reflection, clearly reveals that SF defects extend to the particle surface (Figure 5c), where they create highly active sites. It was previously reported that the laser fluence can affect the abundance of crystalline imperfections. For example, ns laser ablation of Ag in water led to the formation of highly-strained Ag nanocatalyst with a high density of stacking faults, which were active for hydrogen generation [71]. The EDX spectrum in Figure 5d confirms the presence of NiO (shells), based on the atomic Ni:O ratio of ~2:1 (note the different sensitivity of EDX to Ni and O). Similar as the impregnated NPs discussed above, the NP surface seems dominated by Ni/NiO$_x$ ensembles.

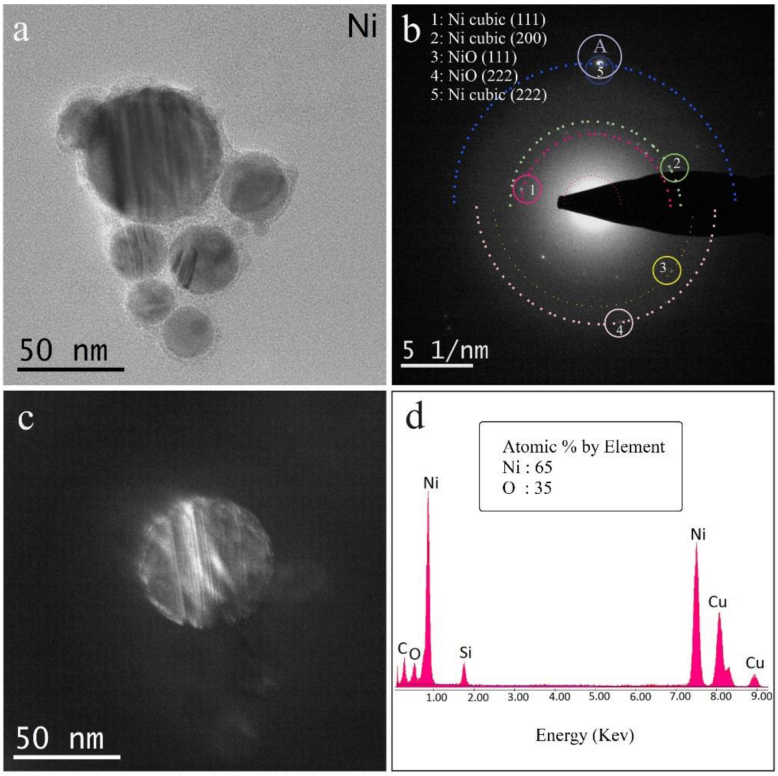

Figure 5. (**a**) TEM bright-field image of Ni NPs laser-synthesized in ethanol, N = 1000, F = 663 J cm^{-2}; (**b**) Selected area electron diffraction pattern of Ni nanoparticles along with evaluated lattice distances and corresponding structures; (**c**) TEM dark-field image of one single Ni NP; (**d**) EDX results of the Ni NPs in (**a**). Adapted with permission from [55]; published by ChemPhysChem, 2017.

In LAL, nucleation occurs within tens of microseconds [44]. Studies on cavitation bubble dynamics [5,44,103,106–108] revealed a formation of primary NPs (~10–20 nm) and secondary NPs (~50–60 nm) resulting from rapid solidification of initial NPs in the low-density mixing region and rupture of the superheated molten layer due to Rayleigh-Taylor instabilities [45]. Secondary nanoparticles (larger NPs) can also be formed by agglomeration of small NPs confined inside a bubble [107,109], due to bubble damping forces towards the bottom of the bubble close to the target. Several processes may lead to larger sizes and asymmetric size distributions, as particle formation may be followed by coalescence or Ostwald ripening. However, based on theoretical kinetic studies, coalescence is favoured for the majority of NPs [110]. Ripening processes can occur after the final collapse of the cavitation bubbles [108].

Different fluids may thus affect particle growth differently. The effect of the type of fluid on the size distribution and polydispersity was studied for Ni/NiO_x NPs, at constant fluence of 663 J cm^{-2} and 1000 pulses (Figure 6 and Table 1) [55]. Compared to the same ablation parameters in ethanol, lower median sizes and IQR values were obtained in isopropanol and butanol, whereas water yielded the broadest distribution. This suggests an effect of laser-induced pyrolysis and photolysis of liquids. During LAL, organic molecules may dissociate on the metallic surface and carbonaceous species can be deposited on the laser-irradiated area. The generated carbonaceous layer increases interfacial absorption, decreasing the ablation threshold fluence and enhancing the incubation effect [56]. Furthermore, agglomeration may be hampered by the formation of a thin graphite shell, acting as capping agent stabilizing smaller colloidal NPs, or of amorphous carbon flakes, inducing steric hindrance [12,72,111].

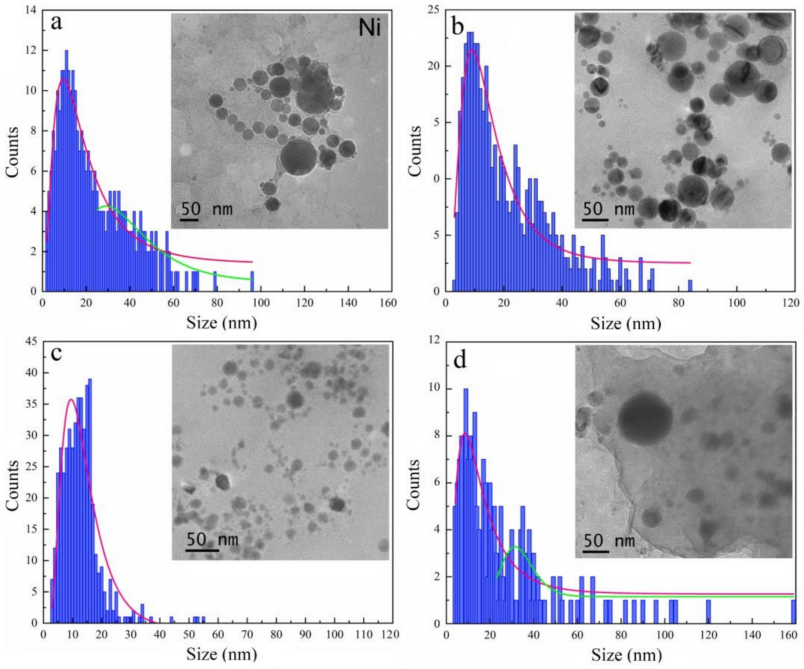

Figure 6. Number weighted size distribution (**a**–**d**) and TEM bright-field images (as inset) of Ni NPs nanosecond laser-synthesized in different fluids (F = 663 J cm^{-2}, N = 1000). (**a**) Ethanol; (**b**) Isopropanol; (**c**) Butanol; (**d**) Water. The red and green lines are LogNormal fits based on the analysis of up to ~500 nanoparticles. Adapted with permission from [55]; published by ChemPhysChem, 2017.

2.3. Femtosecond Laser-Synthesis of Bimetallic (Oxidized) NiAu Nanoparticles

Corresponding ablation experiments were also carried out for a target of Au-coated Ni foil, yielding bimetallic NiAu nanoparticles. Higher ablation efficiency was obtained by fs-pulses at repetition rates ≤ 200 kHz [112], due to a negligible heat affected zone (HAZ) and lower energy losses. Furthermore, the capability of ultrashort pulses for bimetallic nanoparticle synthesis was

explored. Figure 7 shows the influence of the fluid nature on the number-weighted size distribution and polydispersity of fs laser-synthesized (oxidized) NiAu. The distribution analysis revealed a trend similar to that of ns ablation in various fluids, with lowest median sizes and IQR values obtained in isopropanol and butanol (Table 2). Ethanol seemed not to provide the growth-limiting carbonaceous species. Furthermore, EDX analyses of the various nanoparticle samples (Figure 7d; Table 2) revealed a Ni/Au ratio of ~25 and a Ni/O ratio of ~1 in isopropanol and butanol, indicating that Ni was more oxidized in the bimetallic than in the monometallic NPs.

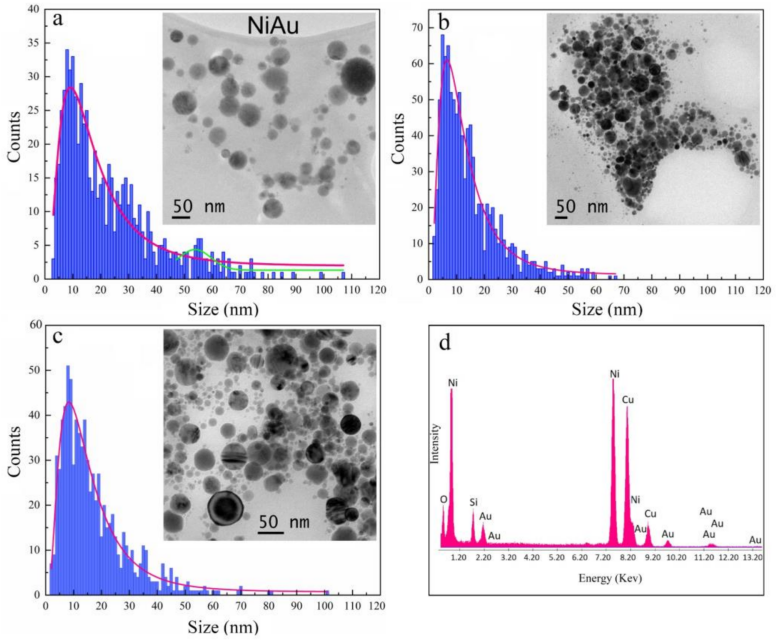

Figure 7. Number weighted size distribution and TEM bright-field images study of bimetallic (oxidized) NiAu NPs synthesized in various fluids by femtosecond laser-ablation (N = 1000, F = 1 J cm^{-2}). (**a**) Ethanol; (**b**) Isopropanol; (**c**) Butanol. (**d**) EDX analyses of bimetallic (oxidized) NiAu NPs in isopropanol. The red and green lines are LogNormal fits based on the analysis of up to 900 nanoparticles. Adapted with permission from [12], published by Springer Nature, 2019.

Table 2. The influence of fluid nature on the size distribution and polydispersity of femtosecond laser-synthesized oxidized NiAu nanoparticles [12] (F = 1 J cm^{-2}, N = 1000,) along with summary of EDX results (atomic%).

Medium	Counted NPs	Mean (nm)	Median (nm)	IQR	Ni (a%)	Au (a%)	O (a%)	Ni/Au	Ni/O
Isopropanol	965	14 ± 11.23	10.9	1.1	56.8	2.5	40.7	22.8	1.4
Butanol	811	17 ± 13.43	13.4	2.3	49.2	1.6	49.2	30.7	1

HRTEM images of the NiAu NPs, fs laser-synthesized in 2-butanol, are shown in Figure 8a,b. Two specific types of nanoparticles were observed (see also Figures 7c and 8d): with and without a graphite shell. The intensity profile displayed as inset in Figure 8b reveals a lattice spacing of 0.333 nm, characteristic of graphite (JCPDS card no. 75-1621). The FFT inset in Figure 8b shows that the NP is single crystalline. However, regions of Ni and Au in a particle cannot be easily differentiated in the current HRTEM images (displaying mostly lattice resolution in one direction). The lattice spacings of cubic Ni (111) (JCPDS card no. 04-0850) and hexagonal Ni (101) (JCPDS card no. 45-1027) are ~0.203 nm and close to Au (200) (JCPDS card no. 00-004-0784). In addition, a NiAu alloy has lattice distances in this region (~0.207 nm for (111); (JCPDS card no. 04-005-1699). Figure 8c displays an SAED pattern, indicating the presence of both Ni and Au (and possibly NiAu alloy), in agreement with EDX.

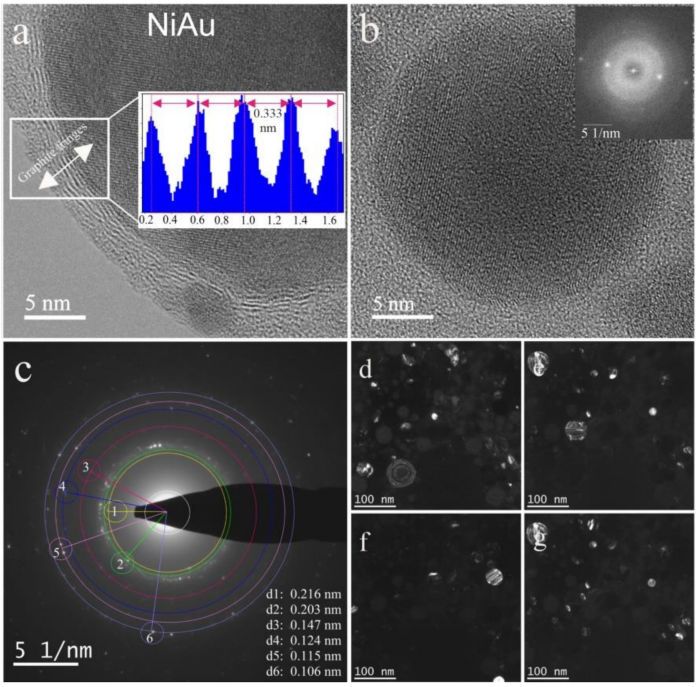

Figure 8. Electron microscopy imaging of bimetallic (oxidized) NiAu NPs synthesized by femtosecond laser in butanol (N = 1000, F = 1 J cm^{-2}). (**a**) HRTEM of single bimetallic (oxidized) NiAu NP (Ni-rich) with a few atomic layers of a graphite shell (intensity profile displayed as inset); (**b**) HRTEM of a single bimetallic (oxidized) NiAu NP (Au-rich); (**c**) Selected area electron diffraction pattern and corresponding dark-field images at various tilted illumination conditions of the electron beam along the 1st and 2nd rings (**d**–**g**). The evaluated lattice distances correspond to the following structures: d1: hexagonal Ni; d2: Cubic Au hexagonal Ni and NiAu alloy; d3: Cubic, monoclinic and hexagonal NiO; d4: Cubic Ni; d5: Hexagonal Ni; d6: Cubic Ni. Adapted with permission from [12], published by Springer Nature, 2019.

Based on previous studies [38], it is reasonable to assume that Au-containing particles do not develop graphite layers. Accordingly, Ni-rich and Au-rich NPs can be differentiated by the existence/absence of graphite layers (Figure 8a,b), that can also be discerned from BF- and DF-images (Figure 8d–g). In fact, Ni NPs can serve as an effective catalyst for carbonization, which is why this is a critical issue in methane reforming processes, as coking triggers poisoning, filament growth, reactor clogging and even catalyst disintegration. Laser-induced pyrolysis of organic molecules on the hot metallic surface [113] may add to the graphitization of Ni NPs. Ultrashort laser pulses induce a series of nonlinear effects that contribute to solvent photoionization [114,115]. Previous studies of laser ablation also reported a graphitization of NPs [12,72] and formation of amorphous carbon networks [42,111,116–119]. Moreover, direct photolysis of solvents due to interaction with an intense beam [116] and thermal pyrolysis of liquid molecules due to formation of high temperature plasma (~5000–7000 K) [120] may occur. Apparently, alloying with Au atoms significantly reduces these unwanted effects, but this should be better controlled. Whether the absence of graphite layers is due to an Au shell or to low-coordinated Ni surface atoms partially replaced by or coordinated to Au atoms will be subject of further studies. The Ni nanoparticles enclosed in a graphite shell also hold promise for studies of catalysis in confined spaces [121,122]).

3. Materials and Methods

3.1. Wet-Chemical Synthesis of ZrO_2 Supported (Oxidized) Ni and NiCu Nanoparticles

ZrO_2 was obtained by calcination of $Zr(OH)_4$ (MEL chemicals XZO 880/01) at 973 K. After calcination, the support has a specific surface area of 36.6 m^2/g. To prepare supported Ni nanoparticles by

impregnation [8,29,75], an appropriate amount of Ni-nitrate to yield 5 wt% loading was dissolved in water, before suspending ZrO_2 powder in the solution and drying at 373 K overnight. The powder was then heated to 723 K in air (heating rate of 5 K/min) and calcined 2 h at 723 K. Before each characterization, the catalyst was oxidized at 773 K and reduced at 673 K (at ~1 bar in 20% O_2 in Ar and 20% H_2 in Ar, respectively, with a flow rate 50 mL/min).

Bimetallic NiCu/ZrO_2 catalysts were synthesized by ZrO_2 co-impregnation with $Cu(NO_3)_2{\cdot}3\ H_2O$ (Fluka, p.a., Vienna, Austria) and $Ni(NO_3)_2{\cdot}6\ H_2O$ (Merck, p.a., Vienna, Austria) [8,29,75]. The nitrate precursor salts were mixed to obtain Ni:Cu molar ratios of 3:1, 1:1 and 1:3 (pure Ni and Cu nanoparticles were prepared as reference), again yielding a metal loading of 5 wt%. For XPS studies another NiCu 3:1 sample with 50 wt% was prepared. Accordingly, the samples are labelled as 31NiCu/ZrO_2, 11NiCu/ZrO_2, 13NiCu/ZrO_2 and 31NiCu/$ZrO_2$50. For other chemical synthesis routes with size, shape and/or interface control, we refer to recent work [123–131].

3.2. Nanosecond Pulsed Laser Ablation of Ni Target in Liquids

A nickel target (Alfa Aesar, Kandel, Germany, 50 × 50 mm^2; thickness of ~2 mm; purity 99.5%) was placed at the bottom of a glassy container, which was closed with an optical quartz window (Figure 9). A Q-switched Nd:YAG laser (SPECTRA-PHYSICS, Vienna, Austria, model no. GCR-130, @532 nm, power of ~1.2 W, pulse duration of 5 ns, repetition rate of 20 Hz, beam diameter ca. 5 mm) was employed to produce Ni NPs in various liquid media (ethanol, isopropanol, butanol, water; Sigma–Aldrich, Vienna, Austria). A power meter (OPHIR Photonics, Darmstadt, Germany) was located after the polarizer (THORLABS, Newton, NJ, USA) to measure the output power. The focal position in various media were experimentally evaluated by microscopically measuring the ablation area on a silicon target (Zeiss AxioVision software, Vienna, Austria) as a function of the distance of the focusing plano-convex lens (focal length of 92 mm) from the target.

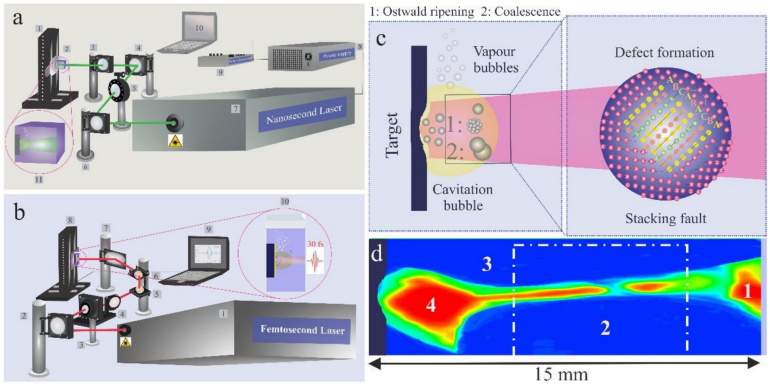

Figure 9. Schematics of the experimental laser ablation apparatus. (**a**) Nanosecond laser set-up: (**1**) motorized XY scanning stage; (**2**) Reactor with optical window; (**3**) Plano-convex lens; (**4**) Reflecting mirror, (**5**) Polarizer with a half-wave plate; (**6**) Reflecting mirror; (**7**) Q-switched Nd:YAG laser, 532nm, 10 Hz, 5 ns; (**8**) Power supply; (**9**) Pulse generator; (**10**) labVIEW controller program; (**11**) ablation cell for nanoparticle synthesis in liquid. (**b**) Femtosecond laser set-up: (**1**) Femtosecond laser system, 800 nm, 1 KHz, 30 fs; (**2**) Mirror; (**3**) Polarizer; (**4**) Beam splitter; (**5** & **6**) Reflecting mirrors; (**7**) Parabolic focusing mirror; (**8**) Target position on motorized XYZ scanning stage, (**9**) CNC controller program and (**10**) Schematic representation of nanoparticle synthesis in liquid (cavitation bubble expansion along with the formation of upward-flow of vapor bubbles). (**c**) Schematics of nanosecond and femtosecond laser-assisted formation of Ni/NiO_x and (oxide) NiAu NPs with a high defect density (stacking faults). This can be attributed to high thermal stresses of primary NPs and rapid cooling of ejected liquid droplets. (**d**) 3D reconstructed image (counter plot) of the nonlinear travel of a Gaussian beam in water (femtosecond laser; E = 250 μJ; N = 1000): (**1**) Kerr effect (laser induced self-focusing); (**2**) Formation of a plasma channel and filamentation (dashed area); (**3**) Diverging section; (**4**) Plasma self-focusing. **b**, **c** Adapted with permission from [72]; published by The Royal Society of Chemistry, 2020.

3.3. Femtosecond Pulsed Laser Ablation of NiAu Target in Liquids

Nickel foil (50 × 50 mm; 0.5 mm thickness; purity ≥ 99.5%) was obtained from Alfa Aesar, Kandel, Germany. Gold wire (purity ≥ 99.95%) was used for physical vapour deposition (PVD) onto the nickel foil. The Au thickness on Ni was evaluated by time-of-flight secondary ion mass spectrometry IONTOF (ToF-SIMS 5), Münster, Germany and a DektakXT stylus profilometer (BRUKER, Karlsruhe, Germany) indicating ~50 nm. Ultrasonication in ethanol was used to clean the surface of the target, which was placed at the back side of the glassy reactor at a height of ~15 mm (Figure 9b). Pure alcohols (ethanol, butanol and isopropanol) were provided by Sigma-Aldrich, Vienna, Austria.

Pulsed laser ablation of NiAu target in fluids was carried out by means of a femtosecond titanium-sapphire (Ti:sapphire) laser (@800 nm, 30 fs, 1 kHz). Laser ablation in liquid was done with horizontal beam transfer to reduce optical fluctuations and variations due to formation of optic cavitation. For amplification, a second (commercial) femtosecond laser (SPECTRA-PHYSICS, Vienna, Austria, ≤400 mW, 800 nm, 10 fs, 75 MHz) was used. The entire system is equipped with a motorized XYZ-scanning stage that was controlled by a bCNC program, San Francisco, CA, USA. In order to modify the output power, a variable atten uator including a beam splitter and a Brewster (thin film) polarizer with quartz half waveplate was used. To measure the final output power, a powermeter (OPHIR Photonics, Darmstadt, Germany) was positioned after a variable attenuator. The focus point in various contact phases was experimentally assessed by microscopically measuring the ablated areas on a silicon target as a function of the distance of a focusing parabolic mirror (focal length of 101.6 mm) to the target. Upon ablation, craters were formed on the target (dimensions depending on the conditions) and thus the laser spot was automatically moved to a pristine area after finishing each sequence. The various components of the femtosecond laser device were described in detail before [12].

3.4. Characterization Techniques (BF-, DF-TEM, SAED, HRTEM, EDX, XPS, IR)

3.4.1. Impregnated Ni and NiCu Nanoparticles

The size, shape and distribution of the metal particles on the zirconia support were determined by high resolution transmission electron microscopy (HRTEM) [130,131]. TEM measurements of catalysts deposited on carbon-coated Au grids were carried out using an analytical field emission TECNAI F20 (200 kV), Hillsboro, OR, USA, equipped with an energy dispersive X-ray fluorescence detector (EDX).

Synchrotron-based near atmospheric pressure NAP-XPS experiments were done at the ISSIS-PGM beamline at the Helmholtz-Zentrum Berlin [8,29,132]. The in situ setup is based on a differentially pumped electrostatic lens system and a SPECS hemispherical electron analyser. To prevent sample charging, the catalyst 31NiCu/$ZrO_2$50 with 50 wt% metal loading was used for the XPS experiments. Measurements at photon energies of 1010 eV for Ni 2p and 1100 eV for Cu 2p yielded a photoelectron kinetic energy of 150 eV, leading to the same probing depth in both cases.

Transmission IR spectra were acquired on a Vertex 70 spectrometer (Bruker, Vienna, Austria), equipped with a mercury cadmium telluride (MTC) detector [29,75,129]. Catalysts were pressed to small discs and placed in the IR cell. Oxidation was carried out in 100 mbar O_2 by heating to 500 °C (10 K min^{-1}) for 1 h. For reduction, the IR cell was evacuated, the catalyst cooled to 300 °C and heated in 5 mbar H_2 and 900 mbar N_2 to 400 °C (30 min), followed by evacuation. All infrared spectra had a resolution of 4 cm^{-1} in the 4000–900 cm^{-1} range, averaging 128 scans to obtain good signal to noise ratio. CO (5 mbar at 30 °C) was used as probe molecule to detect nanoparticle surface composition and oxidation state.

Electronic structure calculations of NiCu alloy nanoparticles of various composition were carried out using the periodic plane-wave code VASP [133] and the PBE [134] exchange-correlation functional. For details we refer to [75,135].

3.4.2. Laser-Synthesized (Oxidized) Ni and NiAu Nanoparticles

Ni/NiO_x and bimetallic (oxidized) NiAu nanoparticles were characterized by transmission electron microscopy (TEM). Samples for TEM imaging were prepared by drop casting of the colloidal dispersion on a lacey carbon film (copper grid) after 5 min ultrasonication, before TEM grids were placed in a vacuum desiccator and dried at room temperature. Bright-field (BF-TEM) and dark-field (DF-TEM) images (particularly detecting defects [136–138]), along with selected area electron diffraction (SAED) patterns, were taken by a Philips CM200 TEM, Hillsboro, OR, USA (LaB_6 cathode, acceleration voltage of 200 kV) equipped with a Gatan Orius CCD camera, Pleasanton, CA, USA. PASAD-tools along with Gatan digital micrograph software were applied to evaluate reciprocal lattice distances and acquire crystallographic data [68]. The measured lattice distances were compared to those in a database [139]. Number-weighted size distributions of nanoparticles were obtained by evaluation of at least seven TEM frames (700 × 700 nm; ca. 500 particles) using Gatan microscopy software. Elemental composition studies were performed by energy-dispersive X-ray spectroscopy (EDX) in the TEM. Furthermore, high resolution transmission electron microscopy (HRTEM) was performed with a FEI Titan 80-300, Hillsboro, OR, USA equipped with an imaging Cs-corrector.

4. Conclusions

Ni, NiCu and NiAu (oxidized or graphite-coated) nanoparticles were prepared by wet-chemical impregnation or laser ablation in liquid media (LAL). Electron microscopy and diffraction, X-ray fluorescence and photoemission, as well as infrared and density functional theory were used to characterize the (surface) structure and composition of the synthesized nanoparticles. The chemically synthesized bimetallic NiCu nanoparticles initially had Cu-rich surfaces, independent of the original Ni:Cu ratio, but Ni segregated to the surface upon heating and especially reaction. This effect must thus be accounted for in nanoparticle synthesis to reach the desired surface composition under working conditions. Laser ablation allows to prepare nanoparticles with controlled size (median) and a high density of bulk defects, that propagate to the surface, which should be relevant for catalytic applications. The parameters of LAL (pulse length, fluence and type of liquid) can be used to control the resulting particle size distributions and surface structures/compositions. In case of NiAu nanoparticles, either clean (presumably Au-rich) or graphite-covered (presumably Ni-rich) surfaces were obtained. The latter samples may be particularly interesting for further studies of intercalated molecules or catalytic reactions in confined spaces, i.e., in between the metallic surface and the graphite overlayer. Clearly, the properties of LAL-synthesized nanoparticles must be further explored by additional adsorption and catalytic reaction studies, similar to those of the impregnated catalysts, but their defect structure holds promise for beneficial properties.

Author Contributions: All authors listed have made a substantial, direct and intellectual contribution to the work, and approved it for publication. All authors have read and agreed to the published version of the manuscript.

Funding: This research was in part funded by the Austrian Science Fund (FWF), grant numbers I 4434-N and F4502-N16.

Acknowledgments: The authors are grateful for the contributions of coworkers and collaborators, whose names appear in the list of references. G.R. acknowledges also the Open Access Funding by the Austrian Science Fund (FWF) via projects SFB FOXSI and Single Atom Catalysis.

Conflicts of Interest: The authors declare no conflict of interest.

References

1. Jang, W.J.; Shim, J.O.; Kim, H.M.; Yoo, S.Y.; Roh, H.S. A review on dry reforming of methane in aspect of catalytic properties. *Catal. Today* **2019**, *324*, 15–26. [CrossRef]
2. Liu, C.J.; Ye, J.; Jiang, J.; Pan, Y. Progresses in the preparation of coke resistant Ni-based catalyst for steam and CO_2 reforming of methane. *ChemCatChem* **2011**, *3*, 529–541. [CrossRef]

3. Wolfbeisser, A.; Sophiphun, O.; Bernardi, J.; Wittayakun, J.; Föttinger, K.; Rupprechter, G. Methane dry reforming over ceria-zirconia supported Ni catalysts. *Catal. Today* **2016**, *277*, 234–245. [CrossRef]
4. Sachtler, W. Selectivity and rate of activity decline of bimetallic catalysts. *J. Mol. Catal.* **1984**, *25*, 1–12. [CrossRef]
5. Schwank, J. *Bimetallic Catalysts: Discoveries, Concepts, and Applications*; John Wiley & Sons: Hoboken, NJ, USA, 1983. [CrossRef]
6. Toshima, N.; Harada, M.; Yamazaki, Y.; Asakura, K. Catalytic activity and structural analysis of polymer-protected gold-palladium bimetallic clusters prepared by the simultaneous reduction of hydrogen tetrachloroaurate and palladium dichloride. *J. Phys. Chem.* **1992**, *96*, 9927–9933. [CrossRef]
7. Toshima, N.; Wang, Y. Novel preparation, characterization and catalytic properties of polymer-protected Cu/Pd bimetallic colloid. *Chem. Lett.* **1993**, *22*, 1611–1614. [CrossRef]
8. Wolfbeisser, A.; Klötzer, B.; Mayr, L.; Rameshan, R.; Zemlyanov, D.; Bernardi, J.; Föttinger, K.; Rupprechter, G. Surface modification processes during methane decomposition on Cu-promoted Ni–ZrO_2 catalysts. *Catal. Sci. Technol.* **2015**, *5*, 967–978. [CrossRef]
9. Amendola, V.; Amans, D.; Ishikawa, Y.; Koshizaki, N.; Scirè, S.; Compagnini, G.; Reichenberger, S.; Barcikowski, S. Room-temperature laser synthesis in liquid of oxide, metal-oxide core-shells, and doped oxide nanoparticles. *Chemistry* **2020**, *26*, 9206–9242. [CrossRef]
10. Kim, M.; Osone, S.; Yeom, G.Y.; Higashi, H.; Seto, T. Synthesis of nanoparticles by laser ablation: A review. *KONA Powder Part. J.* **2017**, *34*, 80–90. [CrossRef]
11. Zhang, D.; Gökce, B.; Barcikowski, S. Laser synthesis and processing of colloids: Fundamentals and applications. *Chem. Rev.* **2017**, *117*, 3990–4103. [CrossRef]
12. Lasemi, N.; Rentenberger, C.; Pospichal, R.; Cherevan, A.S.; Pfaffeneder-Kmen, M.; Liedl, G.; Eder, D. Femtosecond laser-assisted synthesis of Ni/Au BONs in various alcoholic solvents. *Appl. Phys. A* **2019**, *125*, 544. [CrossRef]
13. Garfinkel, D.A.; Pakeltis, G.; Tang, N.; Ivanov, I.N.; Fowlkes, J.D.; Gilbert, D.A.; Rack, P.D. Optical and magnetic properties of Ag–Ni bimetallic nanoparticles assembled via pulsed laser-induced dewetting. *ACS Omega* **2020**, *5*, 19285–19292. [CrossRef] [PubMed]
14. Bharati, M.S.S.; Byram, C.; Soma, V.R. Femtosecond laser fabricated Ag@Au and Cu@Au alloy nanoparticles for surface enhanced Raman spectroscopy based trace explosives detection. *Front. Phys.* **2018**, *6*, 28. [CrossRef]
15. Nastulyavichus, A.A.; Kudryashov, I.S.; Smirnov, A.N.; Rudenko, A.A.; Kharin, A.Y.; Busleev, I.N.; Zayarny, A.D.; Ionin, A.A.; Kirilenko, A.D.; Brunkov, P.N. Novel approach of controllable stoichiometric fabrication of alloyed Au/Ag nanoparticles by nanosecond laser ablation of thin bi-layered films in water. *Laser Phys. Lett.* **2019**, *16*, 096002. [CrossRef]
16. Kuladeep, R.; Jyothi, L.; Alee, K.S.; Deepak, K.L.N.; Rao, D.N. Laser-assisted synthesis of Au-Ag alloy nanoparticles with tunable surface plasmon resonance frequency. *Opt. Mater. Express* **2012**, *2*, 161–172. [CrossRef]
17. Grade, S.; Eberhard, J.; Jakobi, J.; Winkel, A.; Stiesch, M.; Barcikowski, S. Alloying colloidal silver nanoparticles with gold disproportionally controls antibacterial and toxic effects. *Gold Bull.* **2013**, *47*, 83–93. [CrossRef]
18. Neumeister, A.; Jakobi, J.; Rehbock, C.; Moysig, J.; Barcikowski, S. Monophasic ligand-free alloy nanoparticle synthesis determinants during pulsed laser ablation of bulk alloy and consolidated microparticles in water. *Phys. Chem. Chem. Phys.* **2014**, *16*, 23671–23678. [CrossRef]
19. Amendola, V.; Scaramuzza, S.; Carraro, F.; Cattaruzza, E. Formation of alloy nanoparticles by laser ablation of Au/Fe multilayer films in liquid environment. *J. Colloid Interface Sci.* **2017**, *489*, 18–27. [CrossRef]
20. Chau, J.L.H.; Chen, C.Y.; Yang, C.C. Facile synthesis of bimetallic nanoparticles by femtosecond laser irradiation method. *Arab. J. Chem.* **2017**, *10*, S1395–S1401. [CrossRef]
21. Moniri, S.; Hantehzadeh, M.; Ghoranneviss, M.; Asadabad, M.A. Au-Pt alloy nanoparticles obtained by nanosecond laser irradiation of gold and platinum bulk targets in an ethylene glycol solution. *Eur. Phys. J. Plus* **2017**, *132*, 318. [CrossRef]
22. Tarasenko, N.V.; Butsen, A.V.; Nevar, E.A.; Rozantsev, V.A. Plasma assisted synthesis of bimetallic nanoparticles with laser-aided modification of their structure. *Phys. Chem. Appl. Nanostruct.* **2005**, 501–504. [CrossRef]
23. Machado, T.R.; Macedo, N.G.; Assis, M.; Doñate-Buendia, C.; Mínguez-Vega, G.; Teixeira, M.M.; Foggi, C.C.; Vergani, C.E.; Beltrán-Mir, H.; Andrés, J.; et al. From complex inorganic oxides to Ag–Bi nanoalloy: Synthesis by femtosecond laser irradiation. *ACS Omega* **2018**, *3*, 9880–9887. [CrossRef] [PubMed]

24. Lasemi, N.; Bomatí Miguel, O.; Lahoz, R.; Lennikov, V.V.; Pacher, U.; Rentenberger, C.; Kautek, W. Laser-assisted synthesis of colloidal FeW_xOy and Fe/Fe_xOy nanoparticles in water and ethanol. *ChemPhysChem* **2018**, *19*, 1414–1419. [CrossRef] [PubMed]
25. Muniz-Miranda, M.; Gellini, C.; Giorgetti, E.; Margheri, G. Bifunctional Fe_3O_4/Ag nanoparticles obtained by two-step laser ablation in pure water. *J. Colloid Interface Sci* **2017**, *489*, 100–105. [CrossRef] [PubMed]
26. Echegoyen, Y.; Suelves, I.; Lázaro, M.; Moliner, R.; Palacios, J. Hydrogen production by thermocatalytic decomposition of methane over Ni-Al and Ni-Cu-Al catalysts: Effect of calcination temperature. *J. Power Sources* **2007**, *169*, 150–157. [CrossRef]
27. Ashok, J.; Subrahmanyam, M.; Venugopal, A. Hydrotalcite structure derived Ni–Cu–Al catalysts for the production of H2 by CH4 decomposition. *Int. J. Hydrogen Energy* **2008**, *33*, 2704–2713. [CrossRef]
28. Cangiano, M.D.L.A.; Ojeda, M.; Carreras, A.C.; Gonzalez, J.A.; Ruiz, M.D.C. A study of the composition and microstructure of nanodispersed Cu–Ni alloys obtained by different routes from copper and nickel oxides. *Mater. Charact* **2010**, *61*, 1135–1146. [CrossRef]
29. Wolfbeisser, A.; Kovács, G.; Kozlov, S.M.; Föttinger, K.; Bernardi, J.; Klötzer, B.; Neyman, K.M.; Rupprechter, G. Surface composition changes of CuNi-ZrO_2 during methane decomposition: An operando NAP-XPS and density functional study. *Catal. Today* **2017**, *283*, 134–143. [CrossRef]
30. Li, Y.; Chen, J.; Chang, L.; Qin, Y. The doping effect of copper on the catalytic growth of carbon fibers from methane over a Ni/Al_2O_3 catalyst prepared from Feitknecht compound precursor. *J. Catal* **1998**, *178*, 76–83. [CrossRef]
31. Pérez-Hernández, R.; Mondragón Galicia, G.; Mendoza Anaya, D.; Palacios, J.; Angeles-Chavez, C.; Arenas-Alatorre, J. Synthesis and characterization of bimetallic Cu–Ni/ZrO_2 Nanocatalysts: H_2 production by oxidative steam reforming of methanol. *Int. J. Hydrog. Energy* **2008**, *33*, 4569–4576. [CrossRef]
32. Arán-Ais, R.M.; Rizo, R.; Grosse, P.; Algara-Siller, G.; Dembélé, K.; Plodinec, M.; Lunkenbein, T.; Chee, S.W.; Cuenya, B.R. Imaging electrochemically synthesized Cu_2O cubes and their morphological evolution under conditions relevant to CO_2 electroreduction. *Nat. Commun.* **2020**, *11*, 3489. [CrossRef] [PubMed]
33. Wang, H.; Liu, D.; Xu, C. Directed synthesis of well dispersed and highly active AuCu and AuNi nanoparticle catalysts. *Catal. Sci. Technol* **2016**, *6*, 7137–7150. [CrossRef]
34. Vysakh, A.B.; Babu, C.L.; Vinod, C.P. Demonstration of synergistic catalysis in Au@Ni bimetallic core–Shell nanostructures. *J. Phys. Chem. C* **2015**, *119*, 8138–8146. [CrossRef]
35. Srinoi, P.; Chen, Y.T.; Vittur, V.; Marquez, M.D.; Lee, T.R. Bimetallic nanoparticles: Enhanced magnetic and optical properties for emerging biological applications. *Appl. Sci.* **2018**, *8*, 1106. [CrossRef]
36. Zhang, J.; Oko, D.N.; Garbarino, S.; Imbeault, R.; Chaker, M.; Tavares, A.C.; Guay, D.; Ma, D. Preparation of PtAu alloy colloids by laser ablation in solution and their characterization. *J. Phys. Chem. C* **2012**, *116*, 13413–13420. [CrossRef]
37. Garcia, C.; Truttmann, V.; Lopez, I.; Haunold, T.; Marini, C.; Rameshan, C.; Pittenauer, E.; Kregsamer, P.; Dobrezberger, K.; Stöger-Pollach, M.; et al. Dynamics of Pd dopant atoms inside Au nanoclusters during catalytic CO oxidation. *J. Phys. Chem. C* **2020**, *124*, 23626–23636. [CrossRef]
38. Besenbacher, F.; Chorkendorff, I.; Clausen, B.S.; Hammer, B.; Molenbroek, A.M.; Nørskov, J.K.; Stensgaard, I. Design of a surface alloy catalyst for steam reforming. *Science* **1998**, *279*, 1913–1915. [CrossRef]
39. Niakolas, D.K.; Neofytidis, C.S.; Neophytides, S. Effect of Au and/or Mo doping on the development of carbon and sulfur tolerant anodes for SOFCs—A short review. *Front. Environ. Sci* **2017**, *5*, 78. [CrossRef]
40. Chin, Y.H.C.; King, D.L.; Roh, H.-S.; Wang, Y.; Heald, S.M. Structure and reactivity investigations on supported bimetallic AuNi catalysts used for hydrocarbon steam reforming. *J. Catal.* **2006**, *244*, 153–162. [CrossRef]
41. Barcikowski, S.; Compagnini, G. Advanced nanoparticle generation and excitation by lasers in liquids. *Phys. Chem. Chem. Phys.* **2013**, *15*, 3022–3026. [CrossRef]
42. Amendola, V.; Meneghetti, M. Laser ablation synthesis in solution and size manipulation of noble metal nanoparticles. *Phys. Chem. Chem. Phys.* **2009**, *11*, 3805–3821. [CrossRef] [PubMed]
43. Amans, D.; Cai, W.; Barcikowski, S. Status and demand of research to bring laser generation of nanoparticles in liquids to maturity. *Appl. Surf. Sci.* **2019**, *488*, 445–454. [CrossRef]
44. Lam, J.; Amans, D.; Chaput, F.; Diouf, M.; LeDoux, G.; Mary, N.; Masenelli-Varlot, K.; Motto-Ros, V.; Dujardin, C. γ-Al_2O_3 nanoparticles synthesised by pulsed laser ablation in liquids: A plasma analysis. *Phys. Chem. Chem. Phys.* **2014**, *16*, 963–973. [CrossRef] [PubMed]

45. Shih, C.Y.; Wu, C.; Shugaev, M.V.; He, M. Atomistic modeling of nanoparticle generation in short pulse laser ablation of thin metal films in water. *J. Colloid Interface Sci.* **2017**, *489*, 3–17. [CrossRef] [PubMed]
46. Amendola, V.; Meneghetti, M. What controls the composition and the structure of nanomaterials generated by laser ablation in liquid solution? *Phys. Chem. Chem. Phys* **2013**, *15*, 3027–3046. [CrossRef] [PubMed]
47. Maiman, T.H. Stimulated optical radiation in ruby. *Nat. Cell Biol.* **1960**, *187*, 493–494. [CrossRef]
48. Patil, P.P.; Phase, D.M.; Kulkarni, S.K.; Ghaisas, S.V.; Kanetkar, S.M.; Ogale, S.B.; Bhide, V.G. Pulsed-laser–induced reactive quenching at liquid-solid interface: Aqueous oxidation of iron. *Phys. Rev. Lett.* **1987**, *58*, 238–241. [CrossRef]
49. Mafuné, F.; Kohno, J.Y.; Takeda, Y.; Kondow, T.; Sawabe, H. Formation and Size Control of Silver Nanoparticles by Laser Ablation in Aqueous Solution. *J. Phys. Chem. B* **2000**, *104*, 9111–9117. [CrossRef]
50. Kabashin, A.V.; Meunier, M. Synthesis of colloidal nanoparticles during femtosecond laser ablation of gold in water. *J. Appl. Phys.* **2003**, *94*, 7941. [CrossRef]
51. Brikas, M.; Barcikowski, S.; Chichkov, B.; Račiukaitis, G. Production of nanoparticles with high repetition rate picosecond laser JLMN. *J. Laser Micro/Nanoeng.* **2007**, *2*, 230–233. [CrossRef]
52. Zimmer, K. Laser Processing and Chemistry. *Z. Phys. Chem.* **1999**, *208*, 291–292. [CrossRef]
53. Singh, S.C.; Zeng, H.B.; Guo, C.; Cai, W. *Nanomaterials: Processing and Characterization with Lasers*; Wiley-VCH publication: Weinheim, Germany, 2012.
54. Yang, G. *Laser Ablation in Liquids, Principles and Applications in the Preparation of Nanomaterials*; Pan Stanford Publishing: Stanford, CA, USA, 2012.
55. Lasemi, N.; Pacher, U.; Rentenberger, C.; Bomatí-Miguel, O.; Kautek, W. Laser-assisted synthesis of colloidal Ni/NiO_x core/shell nanoparticles in water and alcoholic solvents. *ChemPhysChem* **2017**, *18*, 1118–1124. [CrossRef] [PubMed]
56. Lasemi, N.; Pacher, U.; Zhigilei, L.; Bomatí-Miguel, O.; Lahoz, R.; Kautek, W. Pulsed laser ablation and incubation of nickel, iron and tungsten in liquids and air. *Appl. Surf. Sci* **2018**, *433*, 772–779. [CrossRef]
57. Rupprechter, G. *Sum Frequency Generation and Polarization–Modulation Infrared Reflection Absorption Spectroscopy of Functioning Model Catalysts from Ultrahigh Vacuum to Ambient Pressure*; Elsevier BV: Amsterdam, The Netherlands, 2007; Volume 51, pp. 133–263.
58. Koper, M.T. Structure sensitivity and nanoscale effects in electrocatalysis. *Nanoscale* **2011**, *3*, 2054–2073. [CrossRef] [PubMed]
59. Vogel, D.; Spiel, C.; Schmid, M.; Stöger-Pollach, M.; Schlögl, R.; Suchorski, Y.; Rupprechter, G. The role of defects in the local reaction kinetics of CO oxidation on low-index Pd surfaces. *J. Phys. Chem. C* **2013**, *117*, 12054–12060. [CrossRef]
60. Datler, M.; Bespalov, I.; Rupprechter, G.; Suchorski, Y. Analysing the reaction kinetics for individual catalytically active components: CO oxidation on a Pd powder supported by Pt foil. *Catal. Lett.* **2015**, *145*, 1120–1125. [CrossRef]
61. Feng, X.; Jiang, K.; Fan, S.; Kanan, M.W. A direct grain-boundary-activity correlation for CO electroreduction on Cu nanoparticles. *ACS Central Sci.* **2016**, *2*, 169–174. [CrossRef]
62. Suchorski, Y.; Rupprechter, G. Local reaction kinetics by imaging. *Surf. Sci.* **2016**, *643*, 52–58. [CrossRef]
63. King, M.E.; Personick, M.L. Defects by design: Synthesis of palladium nanoparticles with extended twin defects and corrugated surfaces. *Nanoscale* **2017**, *9*, 17914–17921. [CrossRef]
64. Cheng, T.; Huang, Y.; Xiao, H.; Goddard, W.A. Predicted structures of the active sites responsible for the improved reduction of carbon dioxide by gold nanoparticles. *J. Phys. Chem. Lett.* **2017**, *8*, 3317–3320. [CrossRef]
65. Suchorski, Y.; Kozlov, S.M.; Bespalov, I.; Datler, M.; Vogel, D.; Budinska, Z.; Neyman, K.M.; Rupprechter, G. The role of metal/oxide interfaces for long-range metal particle activation during CO oxidation. *Nat. Mater.* **2018**, *17*, 519–522. [CrossRef] [PubMed]
66. Bornovski, R.; Huang, L.-F.; Komarala, E.P.; Rondinelli, J.M.; Rosen, B.A. Catalytic enhancement of CO oxidation on $LaFeO_3$ regulated by ruddlesden–popper stacking faults. *ACS Appl. Mater. Interfaces* **2019**, *11*, 33850–33858. [CrossRef] [PubMed]
67. Elechiguerra, J.L.; Reyes-Gasga, J.; José-Yacamán, M. The role of twinning in shape evolution of anisotropic noble metal nanostructures. *J. Mater. Chem.* **2006**, *16*, 3906–3919. [CrossRef]

68. Gammer, C.; Mangler, C.; Rentenberger, C.; Karnthaler, H. Quantitative local profile analysis of nanomaterials by electron diffraction. *Scr. Mater.* **2010**, *63*, 312–315. [CrossRef]
69. Kasatkin, I.; Kurr, P.; Kniep, B.; Trunschke, A.; Schlögl, R. Role of lattice strain and defects in copper particles on the activity of Cu/ZnO/Al_2O_3 Catalysts for Methanol Synthesis. *Angew. Chem. Int. Ed.* **2007**, *46*, 7324–7327. [CrossRef]
70. Behrens, M.; Studt, F.; Kasatkin, I.; Kühl, S.; Hävecker, M.; Abild-Pedersen, F.; Zander, S.; Girgsdies, F.; Kurr, P.; Kniep, B.-L.; et al. The active site of methanol synthesis over Cu/ZnO/Al_2O_3 industrial catalysts. *Science* **2012**, *336*, 893–897. [CrossRef]
71. Li, Z.; Fu, J.Y.; Feng, Y.; Dong, C.K.; Liu, H.; Du, X.W. A silver catalyst activated by stacking faults for the hydrogen evolution reaction. *Nat. Catal.* **2019**, *2*, 1107–1114. [CrossRef]
72. Lasemi, N.; Rentenberger, C.; Liedl, G.; Eder, D. The influence of the fluid nature on femtosecond laser ablation properties of a SiO_2/Si target and synthesis of ultrafine-grained Si nanoparticles. *Nanoscale Adv.* **2020**, *2*, 3991–4002. [CrossRef]
73. Sundaram, S.K.; Mazur, E. Inducing and probing non-thermal transitions in semiconductors using femtosecond laser pulses. *Nat. Mater.* **2002**, *1*, 217–224. [CrossRef]
74. Amans, D.; Diouf, M.; Lam, J.; LeDoux, G.; Dujardin, C. Origin of the nano-carbon allotropes in pulsed laser ablation in liquids synthesis. *J. Colloid Interface Sci.* **2017**, *489*, 114–125. [CrossRef]
75. Anic, K.; Wolfbeisser, A.; Li, H.; Rameshan, C.; Föttinger, K.; Bernardi, J.; Rupprechter, G. Surface spectroscopy on UHV-grown and technological Ni–ZrO_2 reforming catalysts: From UHV to operando conditions. *Top. Catal.* **2016**, *59*, 1614–1627. [CrossRef] [PubMed]
76. Sprunger, P.T.; Besenbacher, F.; Stensgaard, I. STM investigation of the Ni(111)−c(4 × 2)−2CO structure. *Chem. Phys. Lett.* **1995**, *243*, 439–444. [CrossRef]
77. Becker, L.; Aminpirooz, S.; Hillert, B.; Pedio, M.; Haase, J.; Adams, D.L. Threefold-coordinated hollow adsorption site for Ni(111)-c(4×2)-CO: A surface-extended x-ray-absorption fine-structure study. *Phys. Rev. B* **1993**, *47*, 9710–9714. [CrossRef] [PubMed]
78. Dávila, M.E.; Asensio, M.; Woodruff, D.P.; Schindler, K.-M.; Hofmann, P.; Weiss, K.-U.; Dippel, R.; Gardner, P.; Fritzsche, V.; Bradshaw, A.; et al. Structure determination of Ni(111)c(4 × 2)-CO and its implications for the interpretation of vibrational spectroscopic data. *Surf. Sci.* **1994**, *311*, 337–348. [CrossRef]
79. Kasai, P.H.; Bishop, R.J.; McLeod, D. Ligand effects on the redox reactions in nickel- and copper-exchanged zeolites. *J. Phys. Chem.* **1978**, *82*, 279–285. [CrossRef]
80. Kitla, A.; Safonova, O.V.; Föttinger, K. Infrared studies on bimetallic copper/nickel catalysts supported on zirconia and ceria/zirconia. *Catal. Lett.* **2013**, *143*, 517–530. [CrossRef]
81. Souza, M.M.; Aranda, D.A.G.; Schmal, M. Reforming of methane with carbon dioxide over Pt/ZrO_2/Al_2O_3 Catalysts. *J. Catal.* **2001**, *204*, 498–511. [CrossRef]
82. Daturi, M.; Binet, C.; LaValley, J.C.; Galtayries, A.; Sporken, R. Surface investigation on $Ce_xZr_{1-x}O_2$ compounds. *Phys. Chem. Chem. Phys.* **1999**, *1*, 5717–5724. [CrossRef]
83. Mihaylov, M.; Chakarova, K.; Hadjiivanov, K. Formation of carbonyl and nitrosyl complexes on titania- and zirconia-supported nickel: FTIR spectroscopy study. *J. Catal.* **2004**, *228*, 273–281. [CrossRef]
84. Morterra, C.; Giamello, E.; Cerrato, G.; Centi, G.; Perathoner, S. Role of surface hydration state on the nature and reactivity of copper ions in Cu-ZrO_2 catalysts: N_2O decomposition. *J. Catal.* **1998**, *179*, 111–128. [CrossRef]
85. Chen, S.; Zou, H.; Liu, Z.; Lin, W. DRIFTS study of different gas adsorption for CO selective oxidation on Cu-Zr-Ce-O Catalysts. *Appl. Surf. Sci.* **2009**, *255*, 6963–6967. [CrossRef]
86. Zecchina, A. Infrared spectroscopy of adsorbed species on the surface of transition metal oxides. *Spectrochim. Acta Part A Mol. Spectrosc.* **1991**, *47*, 823–824. [CrossRef]
87. Manzoli, M.; Di, M.R.; Boccuzzi, F.; Coluccia, S.; Kaspar, J. CO oxidation over CuO_x-CeO_2-ZrO_2 catalysts: Transient behaviour and role of copper clusters in contact with ceria. *Appl. Catal. B* **2005**, *61*, 192–205. [CrossRef]
88. Dalmon, J.A.; Primet, M.; Martin, G.A.; Imelik, B. Magnetic and infrared study of carbon monoxide chemisorption of silica supported nickel-copper alloys. *Surf. Sci.* **1975**, *50*, 95–108. [CrossRef]
89. Guczi, L.; Stefler, G.; Geszti, O.; Sajó, I.; Pászti, Z.; Tompos, A.; Schay, Z. Methane dry reforming with CO_2: A study on surface carbon species. *Appl. Catal. A Gen.* **2010**, *375*, 236–246. [CrossRef]
90. Triantafyllopoulos, N.; Neophytides, S. Dissociative adsorption of CH_4 on NiAu/YSZ: The nature of adsorbed carbonaceous species and the inhibition of graphitic C formation. *J. Catal.* **2006**, *239*, 187–199. [CrossRef]

91. Chia-Ching, W.; Cheng-Fu, Y. Investigation of the properties of nanostructured Li-doped NiO films using the modified spray pyrolysis method. *Nanoscale Res. Lett.* **2013**, *8*, 33. [CrossRef] [PubMed]
92. Wagner, C.D.; Riggs, W.M.; Davis, L.E.; Moulder, J.F.; Muilenberg, G.E. Handbook of X-ray Photoelectron Spectroscopy C. *Surf. Interface Anal.* **1981**, *3*, 190–195. [CrossRef]
93. Pawelec, B.; Damyanova, S.; Arishtirova, K.; Fierro, J.; Petrov, L. Structural and surface features of PtNi catalysts for reforming of methane with CO2. *Appl. Catal. A Gen.* **2007**, *323*, 188–201. [CrossRef]
94. Jones, S.D.; Neal, L.M.; Hagelin-Weaver, H.E. Steam Reforming of Methanol Using Cu-ZnO Catalysts Supported on Nanoparticle Alumina. *Appl. Catal. B* **2008**, *84*, 631–642. [CrossRef]
95. Ghijsen, J.; Tjeng, L.H.; Van, E.J.; Eskes, H.; Westerink, J.; Sawatzky, G.A.; Czyzyk, M.T. Electronic Structure of Cuprous and Cupric Oxides. *Phys. Rev. B Condens. Matter* **1988**, *38*, 11322–11330. [CrossRef] [PubMed]
96. Liu, Z.; Amiridis, M.D.; Chen, Y. Characterization of CuO supported on tetragonal ZrO_2 catalysts for N_2O decomposition to N_2. *J. Phys. Chem. B* **2005**, *109*, 1251–1255. [CrossRef] [PubMed]
97. Tong, W.; West, A.; Cheung, K.; Yu, K.-M.; Tsang, S.C.E. Dramatic effects of gallium promotion on methanol steam reforming Cu-ZnO catalyst for hydrogen production: Formation of 5 Å copper clusters from Cu-$ZnGaO_x$. *ACS Catal.* **2013**, *3*, 1231–1244. [CrossRef]
98. Chen, L.C.; Lin, S.D. The ethanol steam reforming over Cu-Ni/SiO_2 catalysts: Effect of Cu/Ni ratio. *Appl. Catal. B* **2011**, *106*, 639–649. [CrossRef]
99. Naghash, A.R.; Etsell, T.H.; Xu, S. XRD and XPS Study of Cu-Ni interactions on reduced copper-nickel-aluminum oxide solid solution catalysts. *Chem. Mater.* **2006**, *18*, 2480–2488. [CrossRef]
100. Jung, H.J.; Choi, M.Y. Specific solvent produces specific phase Ni nanoparticles: A pulsed laser ablation in solvents. *J. Phys. Chem. C* **2014**, *118*, 14647–14654. [CrossRef]
101. Safa, M.; Dorranian, D.; Masoudi, A.A.; Matin, L.F. Characterizing nickel oxide nanostructures produced by laser ablation method: Effects of laser fluence. *Appl. Phys. A* **2019**, *125*, 687. [CrossRef]
102. Lasemi, N. Pulsed laser generation of colloidal nickel, iron, and tungsten-iron-oxide alloy core-shell nanoparticles. Ph.D. Thesis, Vienna University, Vienna, Austria, 2017.
103. Ivanov, D.S.; Izgin, T.; Maiorov, A.N.; Veiko, V.P.; Rethfeld, B.; Dombrovska, Y.I.; Garcia, M.E.; Zavestovskaya, I.N.; Klimentov, S.M.; Kabashin, A.V. Numerical investigation of ultrashort laser-ablative synthesis of metal nanoparticles in liquids using the atomistic-continuum model. *Molecules* **2019**, *25*, 67. [CrossRef]
104. Dorranian, D.; Eskandari, A.F. Effect of laser fluence on the characteristics of ZnO nanoparticles produced by laser ablation in acetone. *Mol. Cryst. Liq. Cryst.* **2015**, *607*, 1–12. [CrossRef]
105. Fu, X.; Chen, B.; Tang, J.; Zewail, A.H. Photoinduced nanobubble-driven superfast diffusion of nanoparticles imaged by 4D electron microscopy. *Sci. Adv.* **2017**, *3*, e1701160. [CrossRef]
106. Reich, S.; Schönfeld, P.; Wagener, P.; Letzel, A.; Ibrahimkutty, S.; Gökce, B.; Barcikowski, S.; Menzel, A.; Rolo, T.D.S.; Plech, A. Pulsed laser ablation in liquids: Impact of the bubble dynamics on particle formation. *J. Colloid Interface Sci.* **2017**, *489*, 106–113. [CrossRef] [PubMed]
107. Ibrahimkutty, S.; Wagener, P.; Rolo, T.D.S.; Karpov, D.; Menzel, A.; Baumbach, T.; Barcikowski, S.; Plech, A. A hierarchical view on material formation during pulsed-laser synthesis of nanoparticles in liquid. *Sci. Rep.* **2015**, *5*, 16313. [CrossRef] [PubMed]
108. Wagener, P.; Ibrahimkutty, S.; Menzel, A.; Plech, A.; Barcikowski, S. Dynamics of silver nanoparticle formation and agglomeration inside the cavitation bubble after pulsed laser ablation in liquid. *Phys. Chem. Chem. Phys.* **2013**, *15*, 3068–3074. [CrossRef] [PubMed]
109. Ibrahimkutty, S.; Wagener, P.; Menzel, A.; Plech, A.; Barcikowski, S. Nanoparticle formation in a cavitation bubble after pulsed laser ablation in liquid studied with high time resolution small angle x-ray scattering. *Appl. Phys. Lett.* **2012**, *101*, 103104. [CrossRef]
110. Tiemann, M.; Marlow, F.; Hartikainen, J.; Weiss, Ö.; Lindén, M. Ripening Effects in ZnS Nanoparticle Growth. *J. Phys. Chem. C* **2008**, *112*, 1463–1467. [CrossRef]
111. Amendola, V.; Rizzi, G.A.; Polizzi, S.; Meneghetti, M. Synthesis of gold nanoparticles by laser ablation in toluene: Quenching and recovery of the surface plasmon absorption. *J. Phys. Chem. B* **2005**, *109*, 23125–23128. [CrossRef]
112. Chichkov, B.N.; Momma, C.; Nolte, S.; von Alvensleben, F.; Tünnermann, A. Femtosecond, picosecond and nanosecond laser ablation of solids. *Appl. Physics A* **1996**, *63*, 109–115. [CrossRef]
113. Bychkov, V.; Tyulenin, Y.; Firsova, A.A.; Shafranovsky, E.; Gorenberg, A.; Korchak, V.N. Carbonization of nickel catalysts and its effect on methane dry reforming. *Appl. Catal. A Gen.* **2013**, *453*, 71–79. [CrossRef]

114. Olivié, G.; Giguère, D.; Vidal, F.; Ozaki, T.; Kieffer, J.C.; Nada, O.; Brunette, I. Wavelength dependence of femtosecond laser ablation threshold of corneal stroma. *Opt. Express* **2008**, *16*, 4121–4129. [CrossRef]
115. Riabinina, D.; Chaker, M.; Margot, J. Dependence of gold nanoparticle production on pulse duration by laser ablation in liquid media. *Nanotechnology* **2012**, *23*, 135603. [CrossRef]
116. Hu, A.; Sanderson, J.; Zaidi, A.; Wang, C.; Zhang, T.; Zhou, Y.; Duley, W. Direct synthesis of polyyne molecules in acetone by dissociation using femtosecond laser irradiation. *Carbon* **2008**, *46*, 1823–1825. [CrossRef]
117. Amendola, V.; Riello, P.; Meneghetti, M. Magnetic nanoparticles of iron carbide, iron oxide, iron@iron oxide, and metal iron synthesized by laser ablation in organic solvents. *J. Phys. Chem. C* **2010**, *115*, 5140–5146. [CrossRef]
118. Kwong, H.Y.; Wong, M.H.; Leung, C.W.; Wong, Y.W.; Wong, K.H. Formation of core/shell structured cobalt/carbon nanoparticles by pulsed laser ablation in toluene. *J. Appl. Phys.* **2010**, *108*, 34304. [CrossRef]
119. Cristoforetti, G.; Pitzalis, E.; Spiniello, R.; Ishak, R.; Giammanco, F.; Muniz-Miranda, M.; Caporali, S. Physico-chemical properties of Pd nanoparticles produced by Pulsed Laser Ablation in different organic solvents. *Appl. Surf. Sci.* **2012**, *258*, 3289–3297. [CrossRef]
120. Ilyin, A.; Golik, S.S. Femtosecond laser-induced breakdown spectroscopy of sea water. *Spectrochim. Acta Part B: At. Spectrosc.* **2013**, *87*, 192–197. [CrossRef]
121. Fu, Q.; Bao, X. Confined microenvironment for catalysis control. *Nat. Catal.* **2019**, *2*, 834–836. [CrossRef]
122. Prieto, M.J.; Klemm, H.W.; Xiong, F.; Gottlob, D.M.; Menzel, D.; Schmidt, T.; Freund, H.-J. Water formation under silica thin films: Real-time observation of a chemical reaction in a physically confined space. *Angew. Chem. Int. Ed.* **2018**, *57*, 8749–8753. [CrossRef]
123. Munnik, P.; De Jongh, P.E.; De Jong, K.P. Recent developments in the synthesis of supported catalysts. *Chem. Rev.* **2015**, *115*, 6687–6718. [CrossRef]
124. Copéret, C.; Allouche, F.; Chang, K.W.; Conley, M.P.; Delley, M.F.; Fedorov, A.; Moroz, I.B.; Mougel, V.; Pucino, M.; Searles, K.; et al. Bridging the gap between industrial and well-defined supported catalysts. *Angew. Chem. Int. Ed.* **2018**, *57*, 6398–6440. [CrossRef]
125. Van Deelen, T.W.; Mejía, C.H.; De Jong, K.P. Control of metal-support interactions in heterogeneous catalysts to enhance activity and selectivity. *Nat. Catal.* **2019**, *2*, 955–970. [CrossRef]
126. Mantella, V.; Amoròs, L.C.; Buonsanti, R. Shaping non-noble metal nanocrystals via colloidal chemistry. *Chem. Sci.* **2020**, *11*, 11394–11403. [CrossRef]
127. Rizo, R.; Cuenya, B.R. Shape-controlled nanoparticles as anodic catalysts in low-temperature fuel cells. *ACS Energy Lett.* **2019**, *4*, 1484–1495. [CrossRef] [PubMed]
128. Cui, X.; Li, W.; Ryabchuk, P.; Junge, K.; Beller, M. Bridging homogeneous and heterogeneous catalysis by heterogeneous single-metal-site catalysts. *Nat. Catal.* **2018**, *1*, 385–397. [CrossRef]
129. Föttinger, K.; Schlögl, R.; Rupprechter, G. The mechanism of carbonate formation on Pd–Al_2O_3 catalysts. *Chem. Commun.* **2008**, *3*, 320–322. [CrossRef]
130. Rupprechter, G.; Seeber, G.; Goller, H.; Hayek, K. Structure–activity correlations on Rh/Al_2O_3 and Rh/TiO_2 thin film model catalysts after oxidation and reduction. *J. Catal.* **1999**, *186*, 201–213. [CrossRef]
131. Penner, S.; Wang, D.; Se, D.S.; Rupprechter, G.; Podloucky, R.; Schlögl, R.; Hayek, K. Platinum nanocrystals supported by silica, alumina and ceria: Metal-support interaction due to high-temperature reduction in Hydrogen. *Surf. Sci.* **2003**, *532–535*, 276–280. [CrossRef]
132. Rupprechter, G. 8 Surface vibrational spectroscopy on noble metal catalysts from ultrahigh vacuum to atmospheric pressure. *Annu. Rep. Prog. Chem. Sect. C Phys. Chem.* **2004**, *100*, 237–311. [CrossRef]
133. Kresse, G.; Furthmüller, J. Efficient iterative schemes for ab initio total-energy calculations using a plane-wave basis set. *Phys. Rev. B* **1996**, *54*, 11169–11186. [CrossRef]
134. Perdew, J.P.; Burke, K.; Ernzerhof, M. Generalized gradient approximation made simple. *Phys. Rev. Lett.* **1996**, *77*, 3865–3868. [CrossRef]
135. Kozlov, S.M.; Aleksandrov, H.A.; Goniakowski, J.; Neyman, K.M. Effect of MgO(100) support on structure and properties of Pd and Pt nanoparticles with 49-155 atoms. *J. Chem. Phys.* **2013**, *139*, 084701. [CrossRef]
136. Rodriguez De La Fuente, O.; Borasio, M.; Galletto, P.; Rupprechter, G.; Freund, H.-J. The influence of surface defects on methanol decomposition on Pd(111) studied by XPS and PM-IRAS. *Surf. Sci.* **2004**, *566*, 740–745. [CrossRef]

137. Kaichev, V.V.; Morkel, M.; Unterhalt, H.; Prosvirin, I.P.; Bukhtiyarov, V.I.; Rupprechter, G.; Freund, H.J. C–O bond scission on "defect-rich and perfect" Pd (1 1 1)? *Surf. Sci.* **2004**, *566–568*, 1024–1029. [CrossRef]
138. Somorjai, G.A.; Rupprechter, G. The flexible surface: Molecular studies explain the extraordinary diversity of surface chemical properties. *J. Chem. Educ.* **1998**, *75*, 161. [CrossRef]
139. Yibin, X.; Masayoshi, Y.; Pierre, V. Inorganic materials database for exploring the nature of material. *Jpn. J. Appl. Phys.* **2011**, *50*, 11RH02.